Post-Print

Constructing Ballistic Capture Orbits in the Real Solar System Model

Z.-F. Luo · F. Topputo · F. Bernelli-Zazzera · G.-J. Tang

Abstract A method to design ballistic capture orbits in the real solar system model is presented, so extending previous works using the planar restricted three-body problem. In this generalization a number of issues arise, which are treated in the present work. These involve reformulating the notion of stability in three-dimensions, managing a multi-dimensional space of initial conditions, and implementing a restricted n-body model with accurate planetary ephemerides. Initial conditions are categorized into four subsets according to the orbits they generate in forward and backward time. These are labelled weakly stable, unstable, crash, and acrobatic, and their manipulation allows us to derive orbits with prescribed behavior. A post-capture stability index is formulated to extract the ideal orbits, which are those of practical interest. Study cases analyze ballistic capture about Mercury, Europa, and the Earth. These simulations show the effectiveness of the developed method in finding solutions matching mission requirements.

1 Introduction

Ballistic capture orbits have been receiving increased attention throughout the past two decades due to their flexibility in providing multiple insertion opportunities and their capability in reducing fuel requirements (Circi and Teofilatto 2001; Yagasaki 2004; Topputo 2013). Compared to the classic hyperbolic approaches, ballistic capture reduces the excess velocity, and generates orbits requiring less insertion costs. In principle, insertion maneuvers can even be avoided if temporary capture orbits about the target body are accepted. A strategy relying on ballistic capture may also exploit multiple close passages, so mitigating the risks

Z.-F. Luo
Ph.D. Candidate
College of Aerospace Science and Engineering
National University of Defense Technology, Changsha, 410073, P. R. of China
E-mail: luozongfu200@nudt.edu.cn

F. Topputo
Assistant Professor
Department of Aerospace Science and Technology, Politecnico di Milano
Via La Masa, 34 – 20156, Milano, Italy
E-mail: francesco.topputo@polimi.it

F. Bernelli-Zazzera
Full Professor
Department of Aerospace Science and Technology, Politecnico di Milano
Via La Masa, 34 – 20156, Milano, Italy
E-mail: franco.bernelli@polimi.it

G.-J. Tang
Full Professor
College of Aerospace Science and Engineering
National University of Defense Technology, Changsha, 410073, P. R. of China
E-mail: tangguojian@nudt.edu.cn

associated to single-point failures, typical of hyperbolic approaches. The price to pay is a generally longer time to approach the target. Ballistic capture enabled the rescue of Hiten (Belbruno and Miller 1993), was used in SMART-1 (Schoenmaekers et al. 2001), and was the baseline solution in GRAIL (Chung et al. 2010). It has also been proposed in BepiColombo (Jehn et al. 2004), Lunette (Elliot and Alkalai 2011), and ESMO (Vetrisano et al. 2012) .

Ballistic capture arises in n-body models, with $n \geq 3$, therefore a restricted three-body problem suffices to reproduce such mechanism. As no analytic solutions exist in these models, direct numeric simulations are employed. Based on a geometric, energetic definition of stability, a number of recent works have studied the sets composed by the stable initial conditions. In Belbruno (2004), the planar circular restricted-three body problem (CRTBP) was used, along with an algorithmic definition tracking the particle Kepler energy and its first return on a radial segment emanating from the smaller primary. This definition was revisited in García and Gómez (2007), and connections with the invariant manifolds of the CRTBP were sought (see also Fantino et al. (2010)). An efficient method to derive the stable sets was given in Topputo and Belbruno (2009), and their connections with the stable manifolds of the CRTBP was proven in Belbruno et al. (2010, 2013) under certain conditions on mass ratio and energy. A method to derive ballistic capture orbits with prescribed behavior was formulated in Hyeraci and Topputo (2010) within the framework of the planar elliptic restricted three-body problem (ERTBP). In the same model, the effect of primaries' true anomaly was treated in Hyeraci and Topputo (2013); the effect of planetary eccentricity was instead assessed in Circi and Teofilatto (2005). The appropriateness of the CRTBP to study the ballistic capture dynamics was questioned in Makó and Szenkovits (2004). Stable and unstable orbits about Mercury were analyzed in Makó et al. (2010) and Makó (2014) within the ERTBP. The topological properties of the stable sets were studied in Ceccaroni et al. (2012) . Methods to apply the stable sets for lunar capture where studied in Sousa Silva and Terra (2012a), and their boundaries were characterized in Sousa Silva and Terra (2012b). The same task was done in Romagnoli and Circi (2009) and Circi (2012) within a four-body context.

Although some light was shed by the above-mentioned works, some issues still prevent using the ballistic capture in a real, applied context. This involves, in primis, the model in which the ballistic capture orbits are found. If, on the one hand, the restricted three- and four-body models are much more accurate than the classic two-body problem, on the other hand, they still embed some forms of approximation, which cause their orbits to deviate from those arising in the real solar system dynamics. Moreover, a planar analysis is only adequate to infer qualitative information, but fails in providing practical solutions in the real model.

This paper revisits the methodology used to construct the stable sets in a way that attempts to fill the gap between theory and practice. The aim is to bring the concept of ballistic capture to a level of maturity to enable a systematic derivation of practical orbits in applied contexts. This is done in a high-fidelity framework where the three-dimensional, restricted n-body problem with accurate planetary ephemeris is modeled. The main contributions of the paper are: 1) The formulation of a spatial stability condition in a target-centered inertial frame that tracks the "true" number of revolutions, which prevents discrepancies in the number of revolutions between the rotating and the inertial frame (Hyeraci and Topputo 2010), does not require integrating two dynamics (centered at both primaries) to detect instability (Topputo and Belbruno 2009), and avoids changing the reference frame to compute the Kepler energy (García and Gómez 2007; Makó et al. 2010); 2) The design of an algorithm able to extract solutions with a prescribed behavior (capture, escape, impact) from the characterized sets of initial conditions; 3) The introduction of a post-capture stability index to filter ideal orbits from the capture set (Hyeraci and Topputo 2013).

The paper is organized as follows. Section 2 provides background notions, including reference frames and equations of motion. Section 3 introduces the concept of spatial stability along with the methodology developed. Study cases are treated in Section 4, which involve ballistic capture orbits about Mercury, Europa, and the Earth. Final remarks are given in Section 5.

2 Dynamical Model

For the analysis below it is convenient to define the 'target' and the 'primary'. The target, of mass m_t, is the body around which the ballistic capture is studied. The primary, of mass m_p, is the main body around which the target revolves. The mass ratio of the system is $\mu = m_t/(m_t + m_p)$. The list of targets and their primaries considered in this work can be found in Table 2.
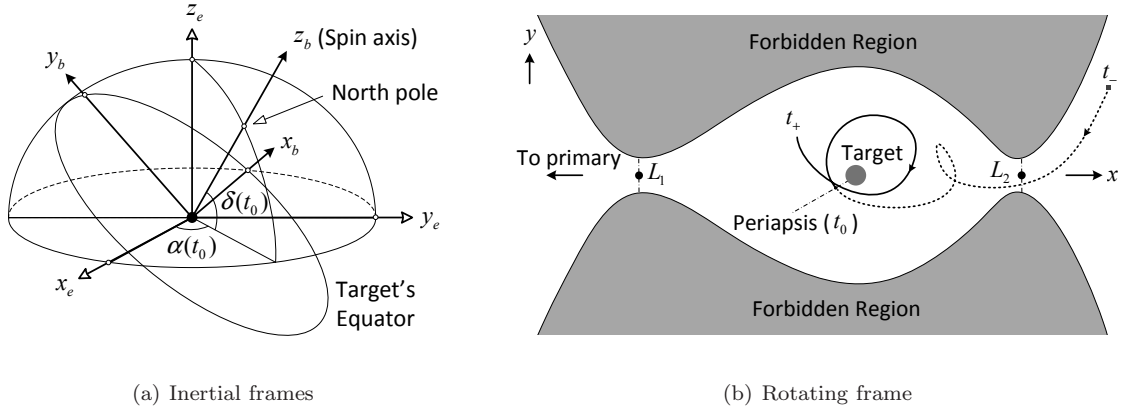
(a) Inertial frames

(b) Rotating frame

Fig. 1 Geometry of reference frames. (left) Inertial frames; (right) Rotating frame.

2.1 Reference Frames

In this work, the precise states of the Sun, planets, and other bodies in the Solar System are extracted from the JPL planetary ephemerides DE430 (Folkner et al. 2014). This model is defined in the Earth mean equator and equinox of J2000 (EME2000 from now on) reference frame (Archinal 2011) [1]. The EME2000 can be centered either at the Earth or at any target body; its axes are labelled (x_e, y_e, z_e), see Fig. 1(a).

In order to control the post-capture orbital parameters, a body mean equator at epoch (BME@Epoch) frame is defined. This reference frame is centered at the target. It is labelled (x_b, y_b, z_b). With reference to Fig. 1(a), the z_b-axis is aligned with the target spin axis, the x_b-axis points to the ascending node of the Earth mean equator, and the y_b-axis completes the dextral orthonormal triad. The target spin axis direction is given in the EME2000 through the right ascension α and declination δ. Accurate values of $\alpha(t)$, $\delta(t)$ as function of the epoch t have been obtained through the model in Archinal (2011). The transformation from the BME@Epoch to EME2000 is

$$\begin{pmatrix} x_e \\ y_e \\ z_e \end{pmatrix} = \begin{bmatrix} -\sin\alpha(t) & -\cos\alpha(t)\sin\delta(t) & \cos\alpha(t)\cos\delta(t) \\ \cos\alpha(t) & -\sin\alpha(t)\sin\delta(t) & \cos\delta(t)\sin\alpha(t) \\ 0 & \cos\delta(t) & \sin\delta(t) \end{bmatrix} \begin{pmatrix} x_b \\ y_b \\ z_b \end{pmatrix} = Q_{b\to e}(t) \begin{pmatrix} x_b \\ y_b \\ z_b \end{pmatrix}. \tag{1}$$

The trajectories can also be shown in a barycentric pulsating rotating (BPR) frame, where both the primary and the target are at rest on the x-axis. With reference to Fig. 1(b), the x-axis is directed from the primary to the target, the z-axis is aligned with their orbital angular momentum, and the y-axis completes the triad. The origin of the BPR frame is at the primary–target barycenter. The primary and target are located at $(-\mu, 0, 0)$ and $(1-\mu, 0, 0)$, respectively, and their mutual distance is always set to unity, regardless of their motion. The transformation from EME2000 to BPR involves a change of origin, a rotation, and a scaling. Details can be found in Gómez et al. (1993).

2.2 Equations of Motion

The ephemerides of the target, the primary, and the other perturbing bodies are provided by the DE430, jup310, sat360, ura111, nep081, and plu043 packages, which are publicly available [2]. More precisely, the positions and velocities vectors are extracted via the toolkit SPICE [3]. Only the main moons (i.e., the Moon, Jupiter's Galilean moons, Saturn's Titan, Uranus's Titania, Neptune's Triton, and Pluto's Charon) are considered.

---

[1] The ephemerides are defined in the International Celestial Reference Frame (ICRF), which has an infinitesimal discrepancy with respect to the EME2000 (Archinal 2011).

[2] Data available at http://naif.jpl.nasa.gov/pub/naif/generic_kernels/spk/planets/de430.bsp, ~/satellites/jup310.bsp, ~/sat360.bsp, ~/ura111.bsp, ~/nep081.bsp, and ~/plu043.bsp [retrieved 5 May 2014].

[3] Data available at http://naif.jpl.nasa.gov/naif/toolkit.html [retrieved 5 May 2014].

Table 1 Normalization units.

Symbol	Remark	Unit	Comment
MU	Gravity parameter unit	km^3/s^2	Target's gravity parameter
LU	Length unit	km	Target's mean radius
TU	Time unit	s	$\sqrt{(\text{LU}^3/\text{MU})}$
VU	Velocity unit	km/s	LU/TU

Table 2 Physical parameters of target bodies in the solar system. [†] NAIF: Navigation and Ancillary Information Facility (NASA/JPL). The offset between Mars barycenter (ID 4) and Mars mass center (ID 499) is extremely small and is neglected. See http://naif.jpl.nasa.gov/pub/naif/generic_kernels/spk/planets/de430-431.cmt [retrieved 5 May 2014]. [‡] SOI: sphere-of-influence, whose radius is $R_s = \rho \left(m_t/m_p \right)^{2/5}$, where ρ is the mean distance between the target and the primary. [*] The Hill radius is a different definition of SOI; its magnitude is in concordance with the L_1 and L_2 distances in the CRTBP model (Szebehely 1967; Russell 2012).

Body	ID[†] NAIF	Gravity par. μ_t, km^3/s^2	Radius R, km	Primary	Semi-major axis, km	Eccentr.	Period days	Mass ratio μ	SOI[‡] R_s,×R	Hill[*] ×R
Mercury	199	2.203E+04	2,439.7	Sun	5.791E+07	0.2056	88.0	1.660E-07	45.92	90.58
Venus	299	3.249E+05	6,051.8	Sun	1.082E+08	0.0068	224.7	2.448E-06	101.80	166.91
Earth	399	3.986E+05	6,371.0	Sun	1.496E+08	0.0167	365.3	3.003E-06	145.03	235.18
Mars	4	4.283E+04	3,389.5	Sun	2.279E+08	0.0934	687.0	3.227E-07	170.00	318.21
Jupiter	599	1.267E+08	69,911	Sun	7.784E+08	0.0484	4,333	9.537E-04	674.20	759.53
Saturn	699	3.794E+07	58,232	Sun	1.427E+09	0.0542	10,759	2.857E-04	908.34	1,117
Uranus	799	5.795E+06	25,362	Sun	2.871E+09	0.0472	30,685	4.366E-05	2,022	2,764
Neptune	899	6.837E+06	24,622	Sun	4.498E+09	0.0086	60,189	5.151E-05	3,437	4,711
Pluto	999	8.696E+02	1,195.0	Sun	5.906E+09	0.2488	90,465	6.553E-09	2,633	6,666
Moon	301	4.903E+03	1,737.4	Earth	3.844E+05	0.0549	27.32	1.215E-02	38.03	35.41
Io	501	5.960E+03	1,821.5	Jupiter	4.218E+05	0.0040	1.77	4.704E-05	4.28	5.79
Europa	502	3.203E+03	1,560.8	Jupiter	6.711E+05	0.0101	3.55	2.528E-05	6.22	8.75
Ganymede	503	9.888E+03	2,631.2	Jupiter	1.070E+06	0.0015	7.15	7.804E-05	9.25	12.05
Callisto	504	7.179E+03	2,410.3	Jupiter	1.883E+06	0.0070	16.69	5.667E-05	15.63	20.81
Titan	606	8.978E+03	2,574.7	Saturn	1.222E+06	0.0292	15.94	2.366E-04	16.82	20.35
Titania	703	2.269E+02	788.9	Uranus	4.363E+05	0.0011	8.71	3.917E-05	9.54	12.35
Triton	801	1.428E+03	1,352.6	Neptune	3.548E+05	0.0000	5.88	2.088E-04	8.85	10.79
Charon	901	1.058E+02	605.0	Pluto	1.959E+04	0.0002	6.39	1.085E-01	12.48	9.96

The equations of motion for a particle are those of the restricted n-body problem

$$\ddot{\mathbf{r}} + \frac{\mu_t}{r^3}\mathbf{r} = -\sum_{i \in \mathbb{P}} \mu_i \left(\frac{\mathbf{r}_i}{r_i^3} + \frac{\mathbf{r} - \mathbf{r}_i}{\|\mathbf{r} - \mathbf{r}_i\|^3} \right), \tag{2}$$

where $\mathbb{P}$ is a set containing the perturbing bodies (all bodies except for the target), $\mathbf{r}$ and $\mathbf{r}_i$ are the position vectors of the spacecraft and perturbing bodies, respectively, r and r_i are their magnitudes, and μ_t and μ_i are the gravity parameters of the target and perturbed bodies, respectively. Equation (2) is written in the EME2000 frame centered at the target. This is done to avoid precision loss (Russell 2012). Although Eq. (2) recalls a perturbed two-body problem, it will be shown that the right-hand side plays a key role in the ballistic capture dynamics.

Numerical Integration. The dynamics (2) are integrated with a 7$^{\text{th}}$/8$^{\text{th}}$ order Runge–Kutta–Felhberg scheme, with automatic step-size control and integration tolerance set to 10^{-12}. To avoid ill-conditioning, Eq. (2) has been normalized by using the units in Table 1 and the physical parameters in Table 2, where a list of candidate target bodies is reported.

3 Methodology

The adimensional Kepler energy of the spacecraft with respect to the target is given by

$$H_t = \frac{v^2}{2} - \frac{1}{r}, \tag{3}$$

where v is the speed. Computing (3) does not require changing the reference frame (as in García and Gómez (2007); Topputo and Belbruno (2009); Belbruno et al. (2010, 2013); Hyeraci and Topputo (2010); Makó et al. (2010); Sousa Silva and Terra (2012a,b)) since the equations of motion (2) are already integrated in a target-centered frame. The Kepler energy is far from being constant in the strong perturbed environment in which the motion is studied.

3.1 Definition of the Initial Conditions

In three-dimensions, an initial condition is specified through six scalars. In order to control the geometry of the post-capture orbits, the spacecraft is initially placed at the periapsis of an osculating ellipse around the target (García and Gómez 2007; Topputo and Belbruno 2009; Hyeraci and Topputo 2010), so reducing the choice to the periapsis radius r_0, the eccentricity e_0, the inclination i_0, the right ascension of the ascending node (RAAN) Ω_0, and the argument of periapsis ω_0; the semi-major axis of the osculating ellipse is $a_0 = r_0/(1 - e_0)$.

In principle, the initial conditions are found by sampling the five-dimensional space in which the osculating orbital parameters are defined. In practice, the orbital plane of the post-capture orbit can be defined by missions constraints, and therefore i_0 and Ω_0 are given. Moreover, it is convenient to specialize the analysis to a fixed e_0, with $e_0 \in [0.9, 1)$ as suggested by numerical experiments (Hyeraci and Topputo 2010). Thus, only r_0 and ω_0 are sampled to account for different periapsis radii and orbital orientations.

The osculating orbital elements are defined in the BME@t_0 frame, where t_0 is the initial epoch. They are converted in position, velocity vectors through the standard transformation (Battin 1987, p. 125), and then to the EME2000 through (1). Let $\mathbf{x}_0 = (\mathbf{r}_0, \mathbf{v}_0)$ be the initial condition in the EME2000. Equations (2) are integrated to yield $\mathbf{x}(t) = (\mathbf{r}(t), \mathbf{v}(t))$, $t \in [t_0, t_0 \pm T]$, where T is a maximum duration, and the plus/minus sign accounts for forward/backward integration.

3.2 Definition of Spatial Stability

In the planar case, the particle stability can be inferred by studying its intersections with a radial line emanating from the target body (Belbruno 2004; García and Gómez 2007; Topputo and Belbruno 2009). In a spatial framework, a plane must be used (Belbruno and Miller 1993; Makó et al. 2010). In the present analysis, the intersection plane is defined by the position vectors $\mathbf{r} = (x, y, z)$ that satisfy

$$\mathbf{r} \cdot (\mathbf{h}_0 \times \mathbf{r}_0) = 0, \tag{4}$$

where $\mathbf{h}_0 = \mathbf{r}_0 \times \mathbf{v}_0$. In practice, the intersection plane is the plane spanned by the initial position vector and angular momentum.

Remark 1 *The particle performs a complete revolution around the target at time t_1 if the following conditions are all simultaneously satisfied,*

$$\mathbf{r}^{(k)}(t_1) \cdot (\mathbf{h}_0 \times \mathbf{r}_0) = 0, \qquad \mathbf{r}^{(k)}(t_1) \cdot \mathbf{r}_0 > 0, \qquad (\mathbf{v}^{(k)}(t_1) \cdot \mathbf{v}_0)(\mathbf{v}^{(k-1)} \cdot \mathbf{v}_0) > 0, \tag{5}$$

where the superscript (k) counts the number of intersections between the plane and the orbit ($\mathbf{r}^{(0)} = \mathbf{r}_0$, $\mathbf{v}^{(0)} = \mathbf{v}_0$).

The first of (5) states that the particle has returned to the intersection plane at t_1; the second restricts the analysis to the semi-plane of interest, to avoid counting semi-revolutions (see Figure 2(a)); the third kinematic condition is used to prune out multiple intersections associated to incomplete revolutions (see Figure 2(b) where the orbit from $\mathbf{v}_0$ to $\mathbf{v}^{(3)}$ is a complete revolution, while the portion from $\mathbf{v}_0$ to $\mathbf{v}^{(2)}$ is not a revolution, although the first two conditions in (5) are satisfied in both $\mathbf{v}^{(1)}$ and $\mathbf{v}^{(2)}$).
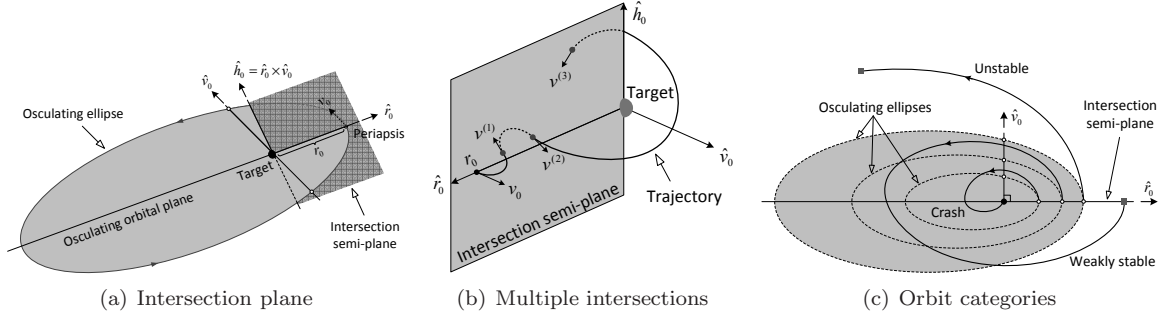
(a) Intersection plane   (b) Multiple intersections   (c) Orbit categories

Fig. 2 Definition of stability.

Remark 2 *The particle escapes from the target at time t_e if the following conditions are simultaneously satisfied*

$$H_t(t_e) > 0, \qquad r(t_e) > R_s, \tag{6}$$

where H_t is the Kepler energy (as defined in (3) *) and R_s is the target sphere of influence (see Table* 2 *).*

Escape occurs when the particle is physically located outside of the target sphere of influence and, at the same time, it possesses positive Kepler energy with respect to the target. This is a conservative condition, which avoids pruning out some weakly stable orbits, deemed of interest, that verify only one of the two inequalities (6) .

Remark 3 *The particle impacts with the target at time t_i if*

$$r(t_i) < R \tag{7}$$

where R is the target mean equatorial radius (see Table 2 *).*

Starting from the periapsis conditions, orbits are integrated forward and their initial conditions are collected into four different sets (see Figure 2(c)). An orbit is said to be 1) *weakly stable* (subset $\mathcal{W}_1$) if the infinitesimal mass performs a complete revolution about the target without escaping from or impacting with it; 2) *unstable* (subset $\mathcal{X}_1$) if the particle escapes from the target; 3) *crash* (subset $\mathcal{K}_1$) if the particle impacts with the target; 4) *acrobatic* (subset $\mathcal{D}_1$) if none of the three previous conditions occurs in the integration time span.

A number of observations arise from the definitions above. 1) The concept of weak stability relies on a geometrical condition only, not requiring checking the energy upon revolution completion (García and Gómez 2007; Topputo and Belbruno 2009; Belbruno et al. 2010, 2013). 2) Instability occurs when conditions (6) hold; this avoids checking for primary interchange escape (García and Gómez 2007; Topputo and Belbruno 2009; Sousa Silva and Terra 2012a,b). 3) Beside colliding with the target, the particle may also collide with one of its natural moons (when the target is the Earth, Jupiter, Saturn, Uranus, Neptune); these initial conditions are ignored, unless otherwise specified. 4) The maximum time duration for the integration is set to $T = 8\pi(R_s)^{3/2}$, which corresponds to four periods of a circular orbit at the SOI; numerical experiments indicated that this interval is sufficiently long to properly categorize the orbits. A group of sample orbits about Mercury (perturbed by the Sun, Jupiter, etc.) is presented in Figure 3.

The definitions above can be applied in backward time as well. In this case, the sets $\mathcal{W}_{-1}$, $\mathcal{X}_{-1}$, $\mathcal{K}_{-1}$, and $\mathcal{D}_{-1}$ are constructed. Multi-revolution sets can also be defined. Let $\mathbf{x}_1 = (\mathbf{r}_1, \mathbf{v}_1)$ (with $\mathbf{r}_1 = \mathbf{r}^{(k)}(t_1)$ and $\mathbf{v}_1 = \mathbf{v}^{(k)}(t_1)$ satisfying (5)) be the terminal point of a one-stable orbit; i.e., an orbit whose initial condition falls in $\mathcal{W}_1$. The state $\mathbf{x}_1$ can then be allocated into one of the four sets $\mathcal{W}_2$, $\mathcal{X}_2$, $\mathcal{K}_2$, and $\mathcal{D}_2$, according to the orbit generated by its forward integration. In general, the set $\mathcal{W}_n$ contains orbits that perform n revolutions about the target without escaping or impacting from it, whereas the sets $\mathcal{X}_n$, $\mathcal{K}_n$, $\mathcal{D}_n$ contain orbits that perform $n-1$ revolutions around the target and then escape, impact, do not return to the semi-plane during the n-th revolution, respectively. If $\mathbb{I}$ is the set of initial conditions, the following relations hold

$$\mathbb{I} = \mathcal{W}_1 \cup \mathcal{X}_1 \cup \mathcal{K}_1 \cup \mathcal{D}_1 = \mathcal{W}_{-1} \cup \mathcal{X}_{-1} \cup \mathcal{K}_{-1} \cup \mathcal{D}_{-1} \quad \text{and} \quad \mathcal{W}_{n-1} = \mathcal{W}_n \cup \mathcal{X}_n \cup \mathcal{K}_n \cup \mathcal{D}_n. \tag{8}$$
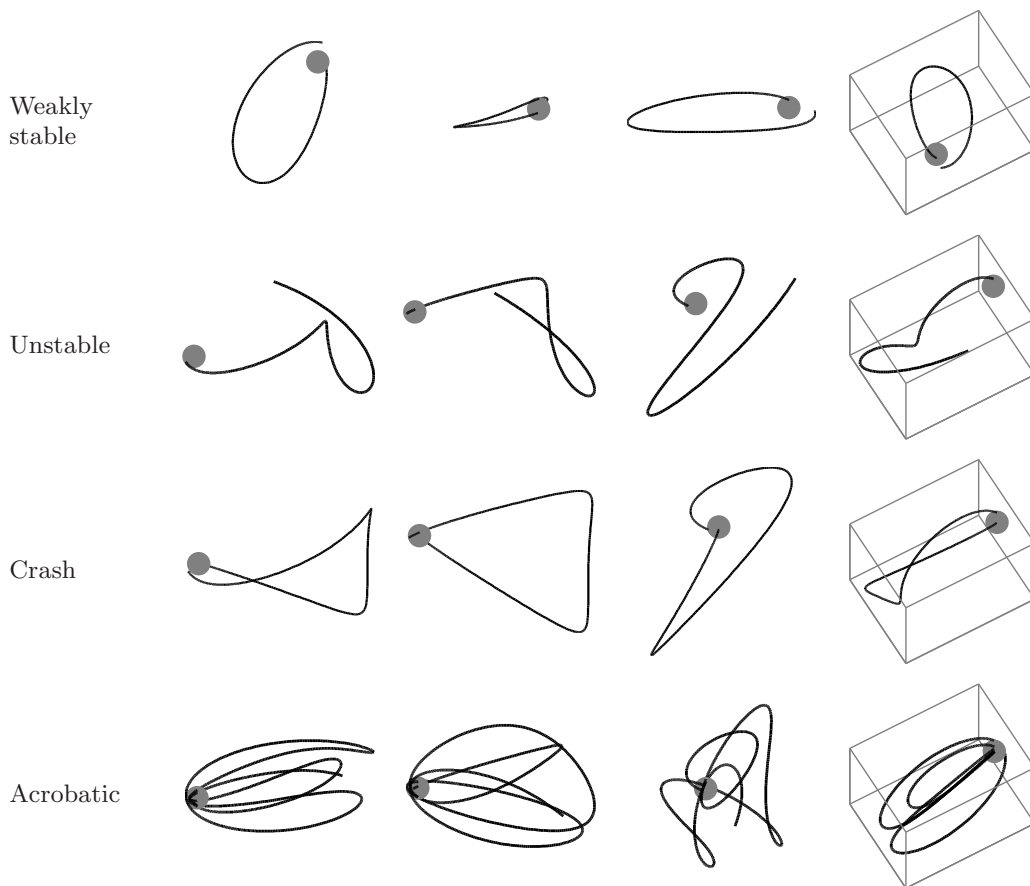
Fig. 3 Sample orbits around Mercury in the EME2000 frame. From left to right the orbits are viewed from positive z-axis, negative y-axis, positive x-axis, and azimuth = 150 deg and elevation = 60 deg. The gray spot is Mercury (not to scale).

3.3 Construction of Ballistic Capture Orbits

Let us now derive practical ballistic capture orbits. Once the sets $\mathcal{W}_n$ (orbits that perform n revolutions about the target body in forward time) and $\mathcal{X}_{-1}$ (orbits that escape the target body in backward time) are computed, the *capture set*, $\mathcal{C}_{-1}^n$, can be derived through

$$\mathcal{C}_{-1}^n = \mathcal{X}_{-1} \cap \mathcal{W}_n. \tag{9}$$

The initial conditions in $\mathcal{C}_{-1}^n$ generate orbits that: 1) escape the target when integrated backward, or equivalently approach the target in forward time coming from outside of its sphere of influence, and 2) perform n revolutions around it without impacting or escaping. This is desirable in preliminary mission analysis, as orbits with this behavior may be good candidates to design a ballistic capture upon arrival. Unlike previous studies in which the capture set is constructed in a three-body context (Hyeraci and Topputo 2010, 2013), in this work $\mathcal{C}_{-1}^n$ is derived in a full-ephemeris, three-dimensional, n-body model, and therefore there is no need to refine the orbits it generates. However, to assure the continuity of the solutions, it is of paramount importance that both $\mathcal{X}_{-1}$ and $\mathcal{W}_n$ in (9) are computed at same initial time t_0 and osculating orbital parameters e_0, i_0, Ω_0.

Escape and Impact Sets. The following two sets can also be achieved as by-product of the computation. The *escape set*, $\mathcal{E}_{-n}^1 = \mathcal{W}_{-n} \cap \mathcal{X}_1$, and the *impact set*, $\mathcal{I}_{-1}^n = \mathcal{X}_{-1} \cap \mathcal{K}_n$. By definition, the escape set contains orbits that perform n revolutions about the primary before escaping from it. Such ballistic escape has been
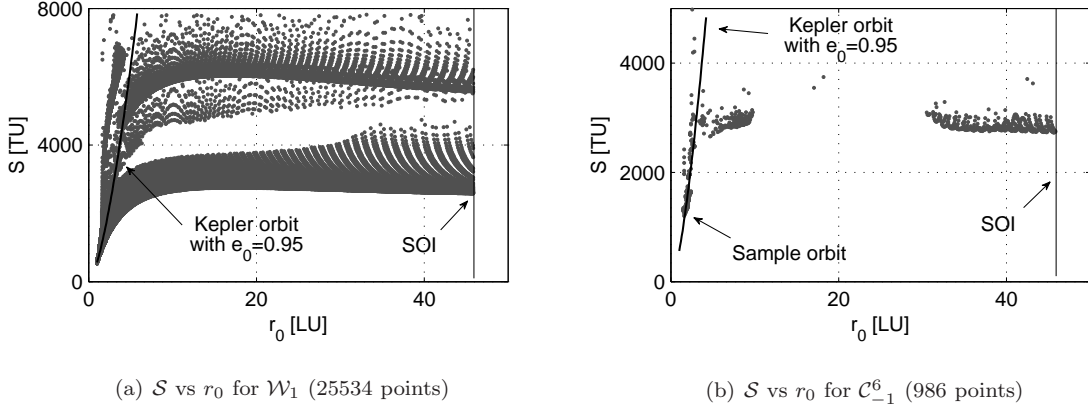
(a) $\mathcal{S}$ vs r_0 for $\mathcal{W}_1$ (25534 points)   (b) $\mathcal{S}$ vs r_0 for $\mathcal{C}_{-1}^6$ (986 points)

Fig. 4 Stability index for solutions in $\mathcal{W}_1$ and $\mathcal{C}_{-1}^6$ about Mercury; $e_0 = 0.95$ (other parameters are given in Section 4.1). The trend of $\mathcal{S}_k$ is superimposed for comparison.

observed in resonant orbits (Belbruno et al. 2008; Topputo et al. 2008). The impact set contains orbits that approach the target from outside of its sphere of influence, perform $n-1$ revolutions around it, and impact with it during the n-th loop; this may be useful in landing missions (Parker 2014). Although they can be useful in many applications, exploiting these two sets is out of the scopes of the present paper.

3.4 Ideal Orbits and Stability Index

In principle, all the orbits in $\mathcal{C}_{-1}^n$ have to be considered when searching for ballistic capture solutions. In practice, most of them are not useful as they give rise to spurious solutions, corresponding to highly unstable trajectories. To discern the useful solutions in $\mathcal{C}_{-1}^n$, the concept of *ideal orbit* is introduced. Ideal orbits are regular, quasi-stable post-capture orbits. For these solutions the particle approaches the target and describes n closed orbits around it with similar shape and orientation. This is desirable in applicative scenarios as it permits to better plan the post-capture phase (Hyeraci and Topputo 2013). The focus is then on filtering the set $\mathcal{C}_{-1}^n$ to extract ideal orbits. In Hyeraci and Topputo (2010), two filters were introduced to identify the incoming branch. In this work, the focus is on the quality of the capture solutions, and therefore the analysis is performed on the post-capture orbit (solid line in Figure 1(b)).

Numerical experiments show that the *stability index*,

$$\mathcal{S} = \frac{t_n - t_0}{n}, \tag{10}$$

embeds sufficient information on the goodness of the post-capture orbits. In (10), t_0 is the initial integration time and t_n is the time at which the n-th revolution is completed. In practice, $\mathcal{S}$ is simply the ratio between the time interval (to complete n revolutions) and the number of revolutions; it is measured in TU (see Table 1). For Keplerian orbits, $\mathcal{S}_k = 2\pi[r_0/(1-e_0)]^{3/2}$, where r_0 and e_0 are the periapsis radius and the eccentricity, respectively. Thus, for any pair (r_0, e_0) in $\mathcal{C}_{-1}^n$, the distance from $\mathcal{S}$ to $\mathcal{S}_k$ measures how much a post-capture orbit is far from being Keplerian. Moreover, for given eccentricity, lower values of $\mathcal{S}$ correspond to orbits with lower periapsis altitudes, which are likely the one sought in practice. It is worth mentioning that $\mathcal{S}$ incorporates the physics of the target-centered motion (target's gravitational parameter and osculating semimajor axis; see the definition of TU in Table 1), and therefore the stability index cannot be compared across different systems. In the remainder, the focus is on ballistic capture solutions with low value of $\mathcal{S}$ and close to $\mathcal{S}_k$.

In Figure 4, the stability index is presented versus the periapsis radius for solutions about Mercury in $\mathcal{W}_1$ and $\mathcal{C}_{-1}^6$. In Figure 5, a sample ballistic capture solution (indicated with the arrow in Figure 4(b)) with low value of $\mathcal{S}$ and close to $\mathcal{S}_k$ is presented. It can be seen that the post-capture revolutions have similar shape and orientation (see Figure 5(a)). A summary of the developed algorithm to construct the sets, manipulate them, and extract the practical solutions is sketched in Figure 6.
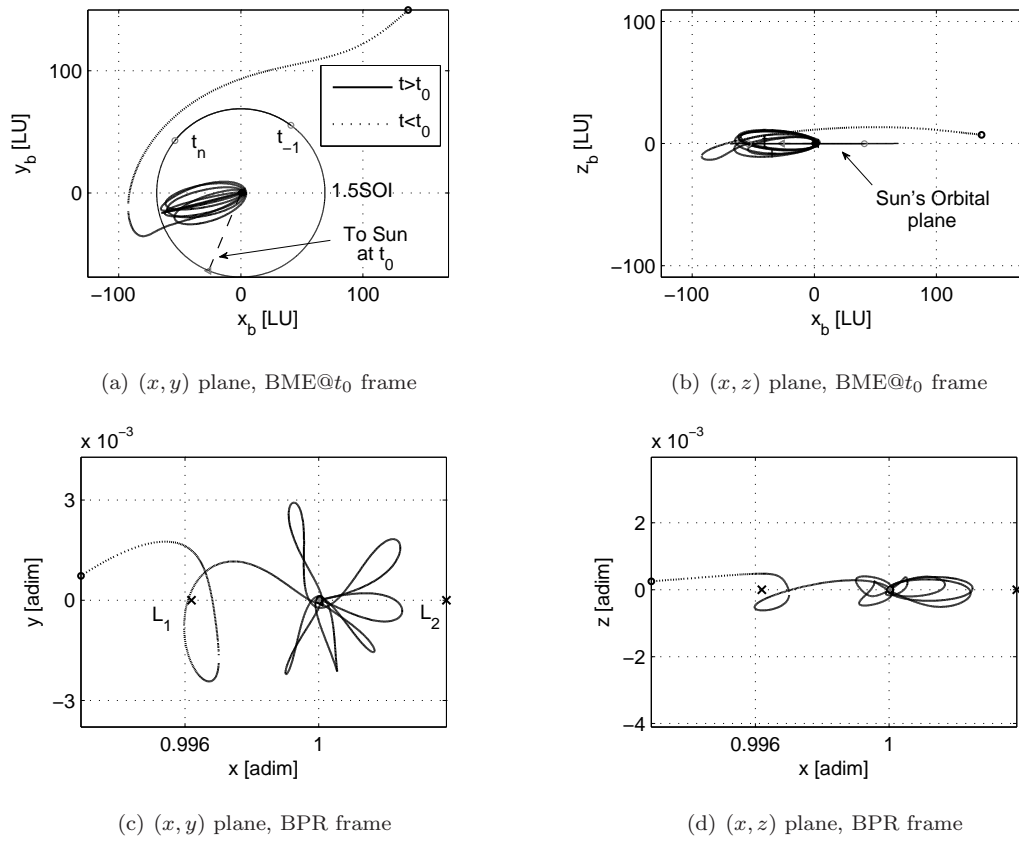
(a) (x, y) plane, BME@t_0 frame

(b) (x, z) plane, BME@t_0 frame

(c) (x, y) plane, BPR frame

(d) (x, z) plane, BPR frame

Fig. 5 The "Sample orbit" in Figure 4(b), $\mathcal{S} =1,204$ TU. The position of the Sun is plotted on a circle with radius equal to 1.5 SOI.

1) **Initialization**
   Select initial epoch t_0 (JD) and ID of target (Table 2)
   Set forward stability number (n) and backward stability number (-1)
   Get transformation matrix from BME@t_0 to EME2000 $(Q_{b \to e}(t_0)$, Eq. (1))
   Set initial eccentricity $(e_0 \in [0.9, 1))$, inclination $(i_0 \in [0, \pi])$, and RAAN $(\Omega_0 \in [0, 2\pi])$
   Discretize periapsis distance, $r_0 \in [R + \epsilon, R_s]$ (Table 2)
   Discretize argument of periapsis, $\omega_0 \in [0, 2\pi]$
   Set maximum integration time T
   Normalize variables (Table 1)
   Select IDs of perturbing bodies (Table 2)
2) **Computation**
   Assign j = current stability number
   IF $j = 1$ OR $j = -1$
      a) Extract current value of r_0 and ω_0
      b) Transform $(t_0, r_0, e_0, i_0, \Omega_0, \omega_0, f_0 = 0)$ to Cartesian state in BME@t_0
      c) Transform the initial state from BME@t_0 to $(\mathbf{r}_0, \mathbf{v}_0)$ in EME2000 with $Q_{b \to e}(t_0)$, Eq. (1)
      d) Forward/backward integrate $(t_0, \mathbf{r}_0, \mathbf{v}_0)$ until (5)/(6)/(7) is verified or $t_0 \pm T$ is reached
      e) Classify the initial conditions and assign it to $\mathcal{W}_j, \mathcal{X}_j, \mathcal{K}_j, \mathcal{D}_j$
   ELSEIF $1 < j \leq n$
      a) Forward integrate the terminal state in $\mathcal{W}_{j-1}$ until (5) is verified or $t_j \pm T$ is reached
      b) Classify the initial conditions and assign it to $\mathcal{W}_j, \mathcal{X}_j, \mathcal{K}_j, \mathcal{D}_j$
   END
3) **Manipulation**
   Extract $\mathcal{C}_{-1}^n$ by intersecting $\mathcal{W}_n$ and $\mathcal{X}_{-1}$ as per (9)
   Eventually construct the escape set $\mathcal{E}_{-n}^1$ and the impact set $\mathcal{I}_{-1}^n$
4) **Analysis**
   Calculate $\mathcal{S}$ for the points in $\mathcal{C}_{-1}^n$ (Eq. (10))
   Draw the $\mathcal{S}_k$ trend and find points nearby with low $\mathcal{S}$
   Reconstruct the ballistic capture solution within $[t_{-1}, t_n]$ by backward and forward integration
   Compute Kepler energy (H_t in (3)) and altitude profiles
   Check approaching direction and overall orbit geometry (osculating plane, close passages, etc.)
   Select desired ballistic capture trajectories according to mission requirements

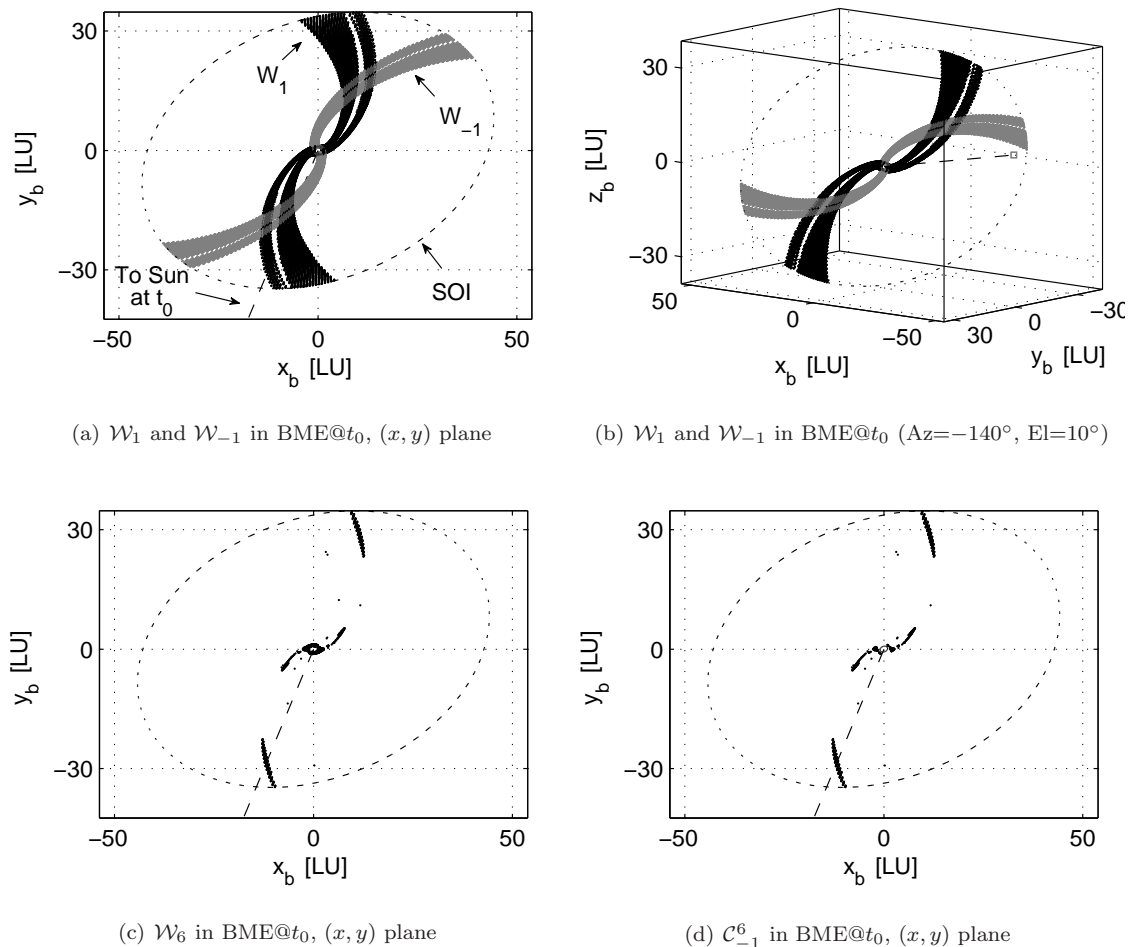**Fig. 6** Algorithm to derive practical ballistic capture solutions.

(a) $\mathcal{W}_1$ and $\mathcal{W}_{-1}$ in BME@t_0, (x, y) plane

(b) $\mathcal{W}_1$ and $\mathcal{W}_{-1}$ in BME@t_0 (Az=$-140°$, El=$10°$)

(c) $\mathcal{W}_6$ in BME@t_0, (x, y) plane

(d) $\mathcal{C}_{-1}^6$ in BME@t_0, (x, y) plane

Fig. 7 Stable and capture sets at Mercury. The number of points in $\mathcal{W}_1$, $\mathcal{W}_{-1}$, $\mathcal{W}_6$, and $\mathcal{C}_{-1}^6$ is 25,534, 19,686, 2,801, and 986, respectively.

4 Study Cases

The methodology developed has been applied to compute ballistic capture solutions at Mercury, Europa, and the Earth. These three targets have been chosen as they are of interest in BepiColombo (Jehn et al. 2004), for a tour of the Jovian moons (Campagnola et al. 2014), and in the context of asteroid retrieval missions (Urrutxua et al. 2014).

4.1 Ballistic Capture at Mercury

The settings for this case are: 1) $t_0 = 2458891.70$ JD (12 February 2020), when Mercury is at the periapsis of its orbit around the Sun (this condition maximizes the chances of finding ideal orbits, see Hyeraci and Topputo (2013)); 2) $e_0 = 0.95$, which is in agreement with the arguments in Hyeraci and Topputo (2010); Circi (2012); 3) $i_0 = 45.04$ deg, $\Omega_0 = 202.50$, which fix the plane of the post-capture orbit; 4) $r_0 \in [R + \epsilon, R_s]$ and $\omega_0 \in [0, 2\pi]$ are uniformly discretized with 548 and 360 points, respectively, so sampling the search space with 197,280 points ($\epsilon = 1$ km); $n = 6$, to be consistent with the analysis in Hyeraci and Topputo (2010). To limit the computational burden while still preserving the high-fidelity of the solutions, the gravitational attractions of the Sun, Venus, Jupiter, and Saturn are considered, besides that of Mercury.

Table 3 Initial conditions in EME2000 for sample solutions with lowest stability index

Target	Position (km)			Velocity (km/s)			$t_{-1} - t_0$	$t_n - t_0$
	x_0	y_0	z_0	v_{x0}	v_{y0}	v_{z0}	days	days
Mercury	3,370.969	1,654.084	803.846	-1.218	2.958	-0.975	-49.08	67.83
Europa	1,270.563	-8,042.341	1,822.657	0.700	0.215	0.460	-0.09	7.32
Earth	-149,771.922	173,040.222	185,160.818	-1.398	-0.608	-0.563	-38.26	59.89

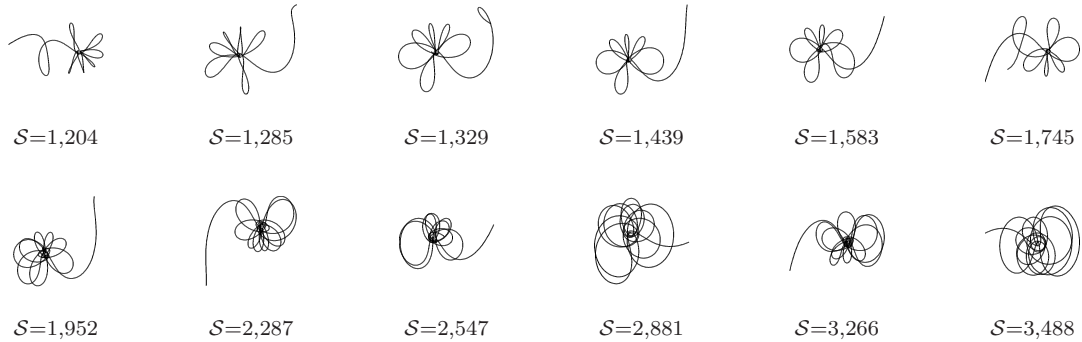(a) Kepler energy w.r.t. Mercury (b) Distance to Mercury (c) Inclination to Mercury's equator
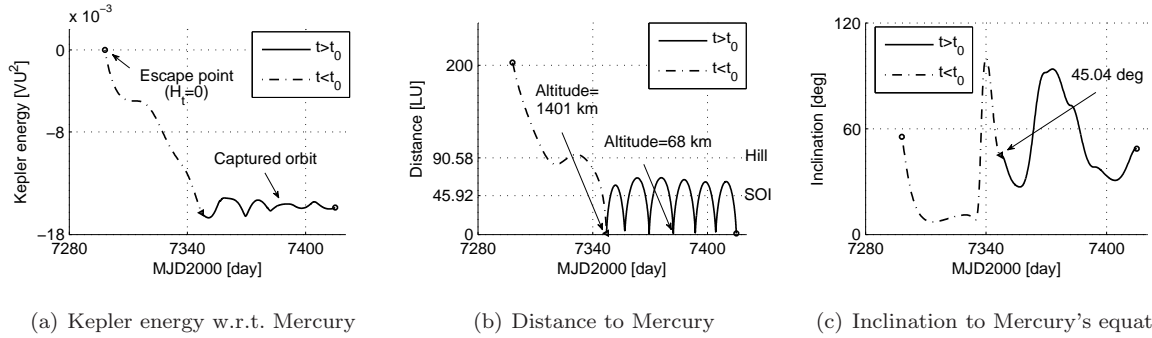
Fig. 8 Kepler energy, distance, and inclination profiles of the sample solution in Figure 5 (backward integration dashed, forward integration solid).

$\mathcal{S}$=1,204 $\mathcal{S}$=1,285 $\mathcal{S}$=1,329 $\mathcal{S}$=1,439 $\mathcal{S}$=1,583 $\mathcal{S}$=1,745

$\mathcal{S}$=1,952 $\mathcal{S}$=2,287 $\mathcal{S}$=2,547 $\mathcal{S}$=2,881 $\mathcal{S}$=3,266 $\mathcal{S}$=3,488

Fig. 9 Ballistic capture orbits about Mercury and their stability index in TU.

Figure 7 shows some stable sets ($\mathcal{W}_{-1}$, $\mathcal{W}_1$, $\mathcal{W}_6$) as well as the capture set $\mathcal{C}_{-1}^6$ at Mercury. It can be noticed that, qualitatively, the structure of the stable sets in the real model recalls that typical of three-/four-body models (García and Gómez 2007; Topputo and Belbruno 2009; Belbruno et al. 2010, 2013; Hyeraci and Topputo 2010, 2013; Makó et al. 2010; Sousa Silva and Terra 2012a,b; Romagnoli and Circi 2009). The set $\mathcal{C}_{-1}^6$ is made up of one third of the points in $\mathcal{W}_6$; most of the difference in these two sets occurs in proximity of Mercury, where orbits tend to be stable, regardless of the direction of integration. The orbit in $\mathcal{C}_{-1}^6$ with the lowest stability index is reported in Figure 5. To allow independent reproduction of the results, the initial condition of this orbit (and for the samples in the other two cases as well) is reported in Table 3. The Kepler energy, distance, and inclination profiles are shown in Figure 8. It can be seen that the algorithm was able to find a solution with regular altitude and energy profiles (Figures 8(a) and 8(b)). The inclination (Figure 8(c)) has instead large variations due to the out-of-plane perturbation from the Sun (see Figure 5(b)). This is acceptable as the present algorithm controls the shape of the post-capture orbit, not its inclination. A number of other solutions are shown in Figure 9 in the BPR frame along with their stability index. It can be seen that the capture orbits are more irregular for increasing $\mathcal{S}$, which demonstrates the validity of this index.
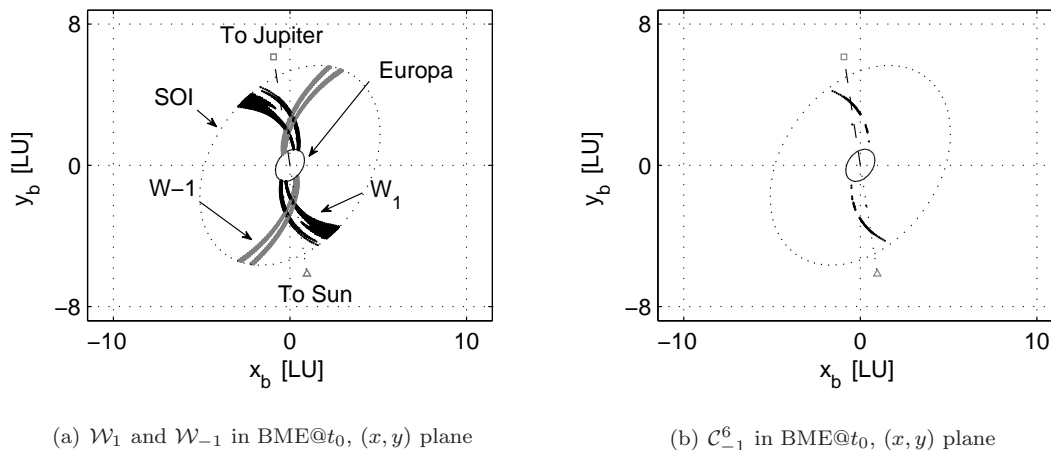
(a) $\mathcal{W}_1$ and $\mathcal{W}_{-1}$ in BME@t_0, (x, y) plane

(b) $\mathcal{C}^6_{-1}$ in BME@t_0, (x, y) plane

Fig. 10 Stable and capture sets at Mercury. The number of points in $\mathcal{W}_1$, $\mathcal{W}_{-1}$, $\mathcal{W}_6$, and $\mathcal{C}^6_{-1}$ is 5,601, 5,410, 190, and 173, respectively.

4.2 Ballistic Capture at Europa

The ballistic capture dynamics at a moon is characterized by the presence of the Sun, a planet and the moon itself (Jupiter and Europa in this case). This is different from planetary capture (e.g., capture at Mercury), where only the Sun and a planet play a major role. Capture trajectories at moons are derived by coupling two restricted three-body problems (with Sun-planet and planet-moon as primaries, see Koon et al. (2001, 2002); Mingotti et al. (2009, 2012)), with consequent increase in complexity. In this work, since the developed algorithm relies on a simple definition of stability, which can be applied about any target body, ballistic capture orbits at Europa are derived in a straightforward way, regardless of their dynamics.

The problem parameters are: $t_0 = 2458852.19$ JD (3 January 2020, when the Sun and Jupiter are in opposition with respect to Europa), $e_0 = 0.95$, $i_0 = 45.00$ deg, $\Omega_0 = 233.82$ deg, $n = 6$. The search space $r_0 \times \omega_0$ is made up of $408 \times 360 = 146,880$ points. The set $\mathbb{P}$ in (2) is made up of the Sun, Jupiter, Saturn, Io, Ganymede, and Callisto. Figure 10 presents the sets $\mathcal{W}_1$, $\mathcal{W}_{-1}$, and $\mathcal{C}^6_{-1}$.

As in the previous case, a sample solution in $\mathcal{C}^6_{-1}$ with the lowest stability index is presented (Figure 11, initial condition in Table 3). The orbit is shown in the BPR frame along with the zero-velocity curves (at t_0). Some features of this solution are shown in Figure 12. Comparing Figure 12 with Figure 8, it can be seen that the escape is here triggered by the distance condition, not by the sign of Keplerian energy as in Figure 8(a); see (6). Also, the backward integration from the first close approach to the escape point is very short (less than 0.1 days, see Table 3). Other ballistic capture orbits with increasing $\mathcal{S}$ are plotted in Figure 13.
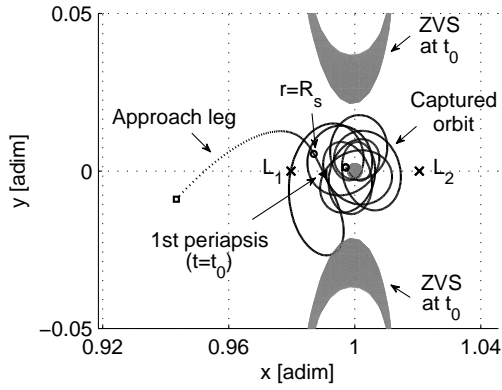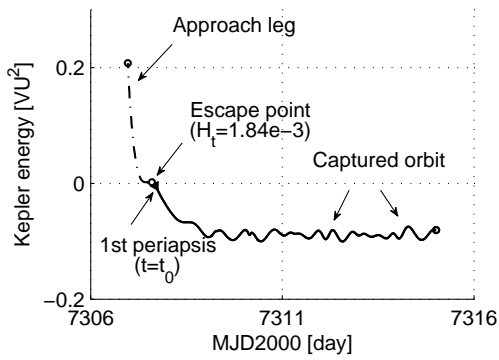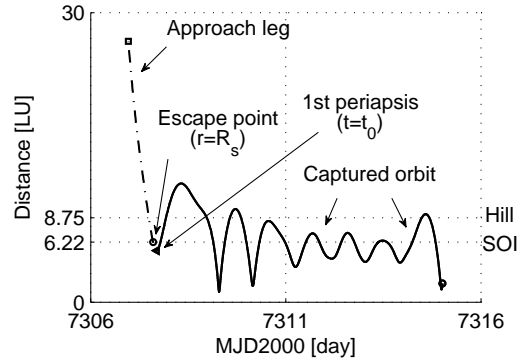
(a) (x, z) plane, BPR frame
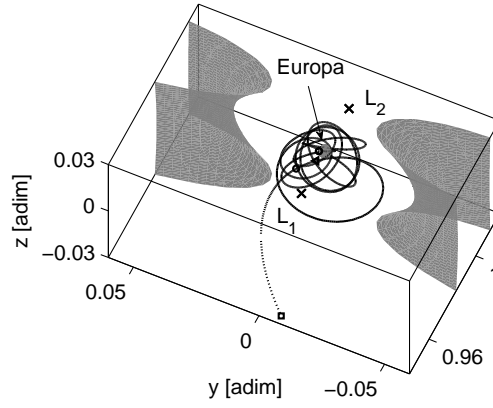
(b) 3D (AZ$=-65°$, El$=56°$)

Fig. 11 Ballistic capture orbit at Europa with lowest stability index ($\mathcal{S} =$96.6 TU). The flight time of the approaching leg (dashed) is -50 TU.

(a) Kepler energy w.r.t. Europa

(b) Distance to Europa

Fig. 12 Kepler energy and distance profiles of the sample solution in Figure 11 (backward integration dashed, forward integration solid).
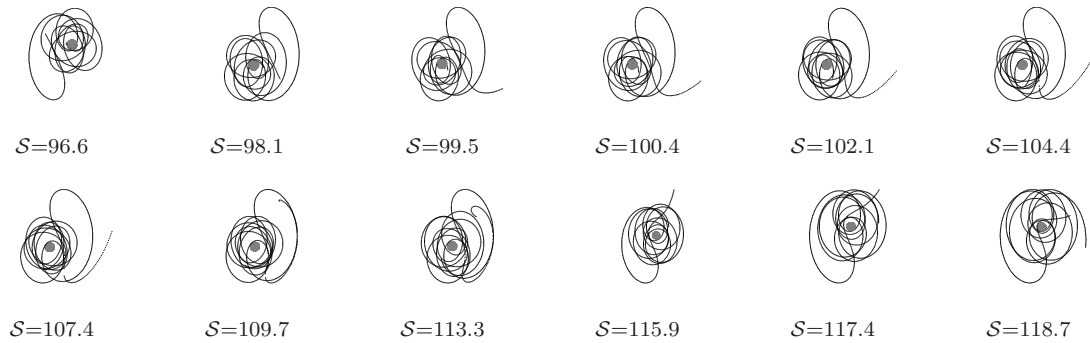

Fig. 13 Ballistic capture orbits about Europa and their stability index in TU.
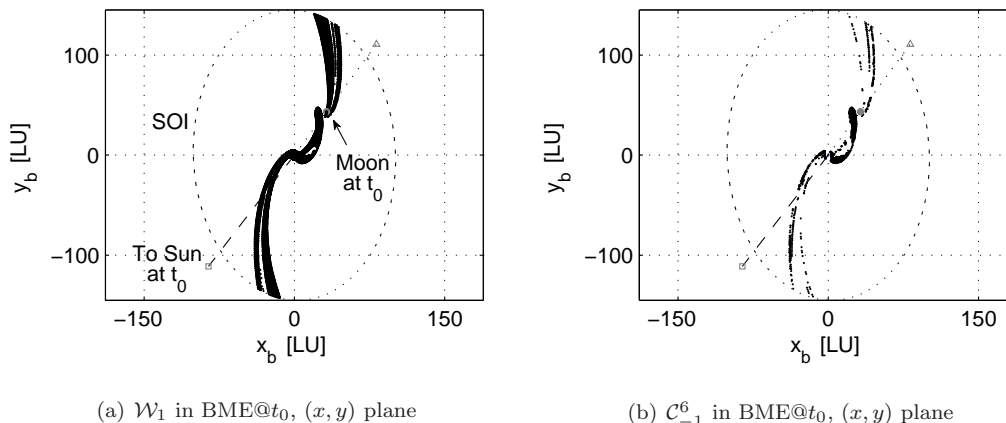
(a) $\mathcal{W}_1$ in BME@t_0, (x, y) plane

(b) $\mathcal{C}^6_{-1}$ in BME@t_0, (x, y) plane

Fig. 14 Stable and capture sets at the Earth. The number of points in $\mathcal{W}_1$, $\mathcal{W}_{-1}$, $\mathcal{W}_6$, and $\mathcal{C}^6_{-1}$ is 55,522, 56,770, 15,363, and 4,498, respectively.

4.3 Ballistic Capture at the Earth

The problem parameters for this case are: $t_0 = 2458888.82$ JD (9 February 2020, when the Sun and the Earth are in opposition with respect to the Moon), $e_0 = 0.95$, $i_0 = 45.89$ deg, $\Omega_0 = 272.54$ deg, $n = 6$. The search space is made up of 919 point for r_0 and 720 points for ω_0 (661,680 initial condition). A finer grid is used in this case to resolve the presence of the Moon (orbits colliding with the Moon are discarded). The gravitational vector field is made up of the Earth, the Sun, the Moon, Jupiter, and Saturn. The stable set $\mathcal{W}_1$ and the capture set $\mathcal{C}^6_{-1}$ are shown in Figure 14. The apparent anomalies in the two sets (upper branch) are due to the presence of the Moon.

The sample trajectory with lowest $\mathcal{S}$ is shown in Figure 15 in both the BME@t_0 and BPR frames (initial conditions in Table 3). It can be seen that a surprisingly regular, ideal post-capture orbit is found thanks to a lunar gravity assist (altitude of 415 km). Figure 16 shows the Kepler energy, the inclination, and distances (to the Earth and the Moon). The influence of the lunar gravity assist can be appreciated in the energy profile (Figure 16(a)). Other solutions with increasing stability indices are shown in Figure 17. These show the major role played by the Moon in stabilizing a particle about the Earth. This mechanism can be used in asteroid retrieval missions.
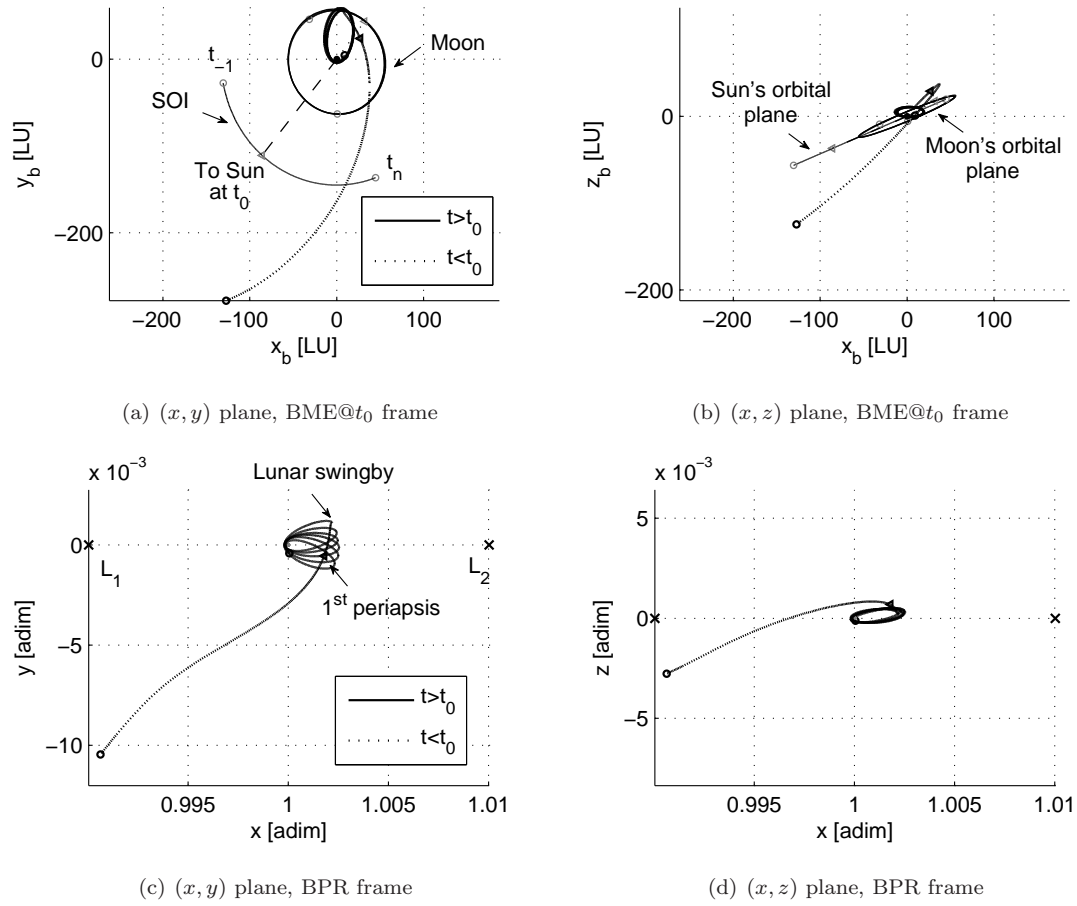
(a) (x, y) plane, BME@t_0 frame

(b) (x, z) plane, BME@t_0 frame

(c) (x, y) plane, BPR frame

(d) (x, z) plane, BPR frame

Fig. 15 Ballistic capture orbit at the Earth with lowest stability index ($\mathcal{S} = 1{,}069$ TU).

(a) Kepler energy w.r.t. the Earth

(b) Inclination to the Earth's equator

(c) Distance to the Earth
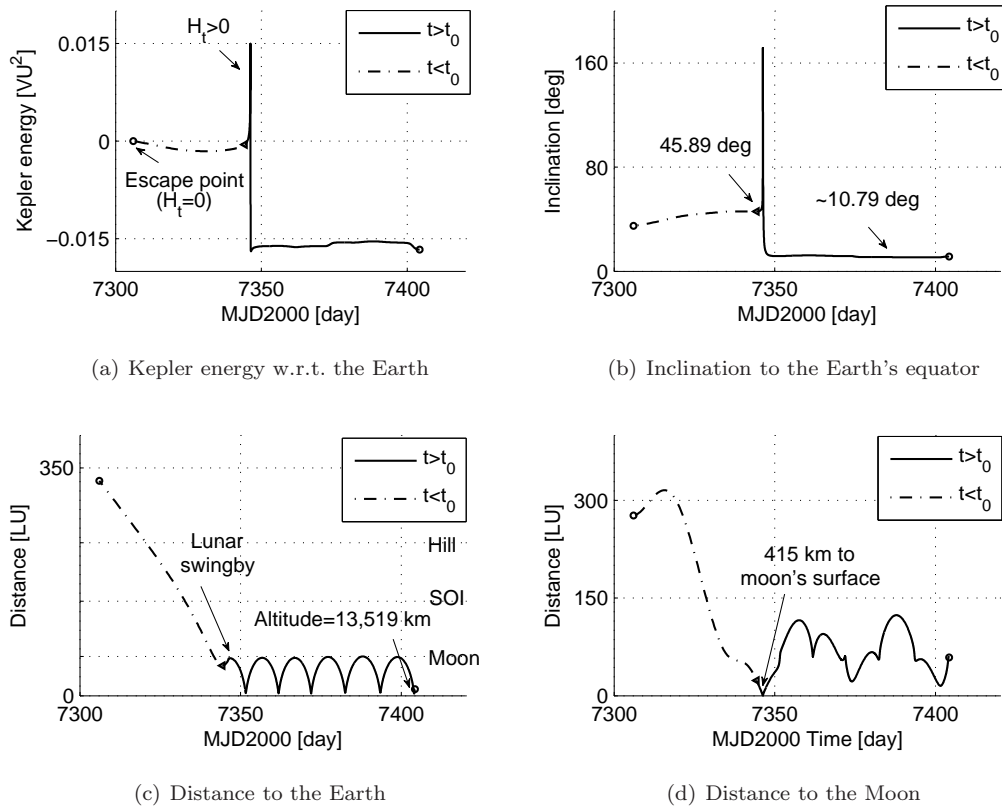
(d) Distance to the Moon

Fig. 16 Parameter histories of the sample orbit in Figure 15.
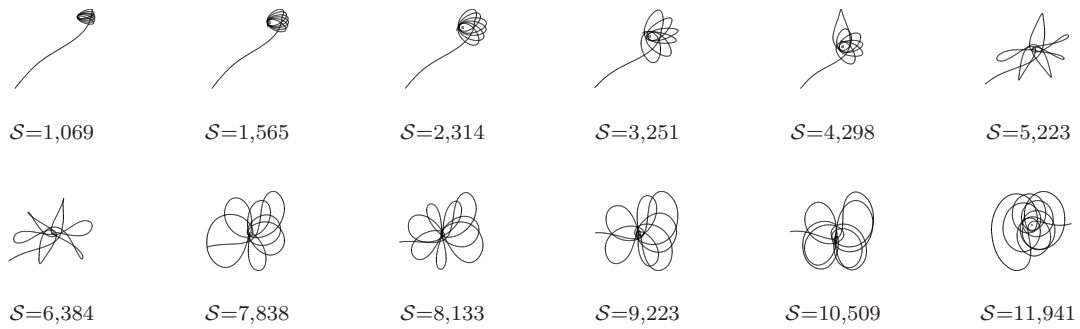

Fig. 17 Ballistic capture orbits about the Earth and their stability index in TU.

5 Conclusions

A systematic method to generate ballistic capture orbits in a three-dimensional, n-body, full ephemeris model is presented in this work. This model is known as the real model due to its adherence to the real solar system dynamics. A novel definition of spatial stability is introduced, which is based on geometric, kinematic arguments. This definition, together with the escape and impact conditions, allows us to categorize the orbits into four sets. Ballistic capture orbits with prescribed behavior are extracted from these sets by simple manipulation. A stability index is formulated and used to detect the ideal orbits. These are regular, quasi-stable post-capture orbits, and therefore they match application requirements. The usefulness of this index is demonstrated through examples. Capture dynamics at Mercury, Europa, and the Earth have been considered as study cases. Numerical results indicate that ideal orbits can be acquired at zeros cost, and the presence of a moon can be profitably exploited to further improve the quality of the post-capture trajectories. This demonstrates the inherent potential possessed by these orbits, for which a future utilization is desirable.

References

Archinal, B. A. et al. 2011. Report of the IAU Working Group on Cartographic Coordinates and Rotational Elements: 2009. *Celestial Mechanics and Dynamical Astronomy* 109 (2): 101–135. doi:10.1007/s10569-010-9320-4.

Battin, R. H. 1987, p. 125. *An Introduction to the Mathematics and Methods of Astrodynamics.* AIAA, New York.

Belbruno, E. 2004. *Capture Dynamics and Chaotic Motions in Celestial Mechanics: With Applications to the Construction of Low Energy Transfers.* Princeton University Press.

Belbruno, E., and J. Miller. 1993. Sun-Perturbed Earth-to-Moon Transfers with Ballistic Capture. *Journal of Guidance, Control, and Dynamics* 16: 770–775. doi:10.2514/3.21079.

Belbruno, E., M. Gidea, and F. Topputo. 2010. Weak Stability Boundary and Invariant Manifolds. *SIAM Journal on Applied Dynamical Systems* 9 (3): 1061–1089. doi:10.1137/090780638.

Belbruno, E., M. Gidea, and F. Topputo. 2013. Geometry of Weak Stability Boundaries. *Qualitative Theory of Dynamical Systems* 12 (1): 53–66. doi:10.1007/s12346-012-0069-x.

Belbruno, E., F. Topputo, and M. Gidea. 2008. Resonance Transition Associated to Weak Capture in the Restricted Three-Body Problem. *Advances in Space Research* 42 (8): 18–39. doi:10.1016/j.asr.2008.01.018.

Campagnola, S., B. Buffington, and A. Petropoulos. 2014. Jovian Tour Design for Orbiter and Lander Missions to Europa. *Acta Astronautica* 100: 68–81. doi:10.1016/j.actaastro.2014.02.005.

Ceccaroni, M., J. Biggs, and L. Biasco. 2012. Analytic Estimates and Topological Properties of the Weak Stability Boundary. *Celestial Mechanics and Dynamical Astronomy* 114 (1–2): 1–24. doi:10.1007/s10569-012-9419-x.

Chung, M. J., S. J. Hatch, J. A. Kangas, S. M. Long, R. B. Roncoli, and T. H. Sweetser. 2010. Trans-Lunar Cruise Trajectory Design of GRAIL (Gravity Recovery and Interior Laboratory) Mission. In *AIAA/AAS Astrodynamics Specialist Conference, AIAA 2010-8384,* 2–5. Toronto, Ontario, Canada.

Circi, C. 2012. Properties of Transit Trajectory in the Restricted Three and Four-Body Problem. *Advances in Space Research* 49 (10): 1506–1519. doi:10.1016/j.asr.2012.02.034.

Circi, C., and P. Teofilatto. 2001. On the Dynamics of Weak Stability Boundary Lunar Transfers. *Celestial Mechanics and Dynamical Astronomy* 79 (1): 41–72. doi:10.1023/A:1011153610564.

Circi, C., and P. Teofilatto. 2005. Effect of Planetary Eccentricity on Ballistic Capture in the Solar System. *Celestial Mechanics and Dynamical Astronomy* 93 (1-4): 69–86. doi:10.1007/s10569-005-3640-9.

Elliot, J., and L. Alkalai. 2011. Lunette: A Network of Lunar Landers for In-Situ Geophysical Science. *Acta Astronautica* 68: 1201–1207.

Fantino, E., G. Gómez, J. Masdemont, and Y. Ren. 2010. A Note on Libration Point Orbits, Temporary Capture and Low-Energy Transfers. *Acta Astronautica* 67 (9–10): 1038–1052. doi:10.1016/j.actaastro.2010.06.037.

Folkner, W. M., J. G. Williams, D. H. Boggs, R. S. Park, and P. Kuchynka. 2014. The Planetary and Lunar Ephemerides DE430 and DE431, Technical report, IPN Progress Report 42-196.

García, F., and G. Gómez. 2007. A Note on Weak Stability Boundaries. *Celestial Mechanics and Dynamical Astronomy* 97: 87–100. doi:10.1007/s10569-006-9053-6.

Gómez, G., A. Jorba, J. Masdemont, and C. Simó. 1993. Study of the Transfer from the Earth to a Halo Orbit around the Equilibrium Point L_1. *Celestial Mechanics and Dynamical Astronomy* 56: 541–562.

Hyeraci, N., and F. Topputo. 2010. Method to design ballistic capture in the elliptic restricted three-body problem. *Journal of Guidance, Control, and Dynamics* 33 (6): 1814–1823. doi:10.2514/1.49263.

Hyeraci, N., and F. Topputo. 2013. The role of true anomaly in ballistic capture. *Celestial Mechanics and Dynamical Astronomy* 116 (2): 175–193. doi:10.1007/s10569-013-9481-z.

Jehn, R., S. Campagnola, D. García, and S. Kemble. 2004. Low-Thrust Approach and Gravitational Capture at Mercury. In *Proceedings of the 18th International Symposium on Space Flights Dynamics*, Vol. 584, 487. Munich, Germany.

Koon, W. S., M. W. Lo, J. E. Marsden, and S. D. Ross. 2001. Low Energy Transfer to the Moon. *Celestial Mechanics and Dynamical Astronomy* 81: 63–73.

Koon, W. S., M. W. Lo, J. E. Marsden, and S. D. Ross. 2002. Constructing a Low Energy Transfer between Jovian Moons. *Contemporary Mathematics* 292: 129–145.

Makó, Z. 2014. Connection between Hill Stability and Weak Stability in the Elliptic Restricted Three-Body Problem. *Celestial Mechanics and Dynamical Astronomy* to appear: 1–19.

Makó, Z., and F. Szenkovits. 2004. Capture in the Circular and Elliptic Restricted Three-Body Problem. *Celestial Mechanics and Dynamical Astronomy* 90: 51–58. doi:10.1007/s10569-004-5899-7.

Makó, Z., F. Szenkovits, J. Salamon, and R. Oláh-Gál. 2010. Stable and Unstable Orbits around Mercury. *Celestial Mechanics and Dynamical Astronomy* 108: 357–370. doi:10.1007/s10569-010-9309-z.

Mingotti, G., F. Topputo, and F. Bernelli-Zazzera. 2009. Low-Energy, Low-Thrust Transfers to the Moon. *Celestial Mechanics and Dynamical Astronomy* 105 (1–3): 61–74. doi:10.1007/s10569-009-9220-7.

Mingotti, G., F. Topputo, and F. Bernelli-Zazzera. 2012. Efficient Invariant-Manifold, Low-Thrust Planar Trajectories to the Moon. *Communication in Nonlinear Science and Numerical Simulation* 17 (2): 817–831. doi:10.1016/j.cnsns.2011.06.033.

Parker, J. 2014. Establishing a Network of Lunar Landers via Low-Energy Transfers. In *24th AAS/AIAA Space Flight Mechanics Meeting, Santa Fe, New Mexico, 26–30 January*, 1–21.

Romagnoli, D., and C. Circi. 2009. Earth–Moon Weak Stability Boundaries in the Restricted Three and Four Body Problem. *Celestial Mechanics and Dynamical Astronomy* 103 (1): 79–103. doi:10.1007/s10569-008-9169-y.

Russell, R. P. 2012. Survey of Spacecraft Trajectory Design in Strongly Perturbed Environments. *Journal of Guidance, Control, and Dynamics* 35 (3): 705–720. doi:10.2514/1.56813.

Schoenmaekers, J., D. Horas, and J. A. Pulido. 2001. SMART-1: With Solar Electric Propulsion to the Moon. In *Proceeding of the 16th International Symposium on Space Flight Dynamics*, 3–7. Pasadena, California.

Sousa Silva, P., and M. Terra. 2012a. Applicability and Dynamical Characterization of the Associated Sets of the Algorithmic Weak Stability Boundary in the Lunar Sphere of Influence. *Celestial Mechanics and Dynamical Astronomy* 113: 141–168. doi:10.1007/s10569-012-9409-z.

Sousa Silva, P., and M. Terra. 2012b. Diversity and Validity of Stable-Unstable Transitions in the Algorithmic Weak Stability Boundary. *Celestial Mechanics and Dynamical Astronomy* 113: 453–478. doi:10.1007/s10569-012-9418-y.

Szebehely, V. 1967. *Theory of Orbits: The Restricted Problem of Three Bodies*. Academic Press Inc..

Topputo, F. 2013. On Optimal Two-Impulse Earth-Moon Transfers in a Four-Body Model. *Celestial Mechanics and Dynamical Astronomy* 117 (3): 279–313. doi:10.1007/s10569-013-9513-8.

Topputo, F., and E. Belbruno. 2009. Computation of Weak Stability Boundaries: Sun–Jupiter System. *Celestial Mechanics and Dynamical Astronomy* 105 (1–3): 3–17. doi:10.1007/s10569-009-9222-5.

Topputo, F., E. Belbruno, and M. Gidea. 2008. Resonant Motion, Ballistic Escape, and their Applications in Astrodynamics. *Advances in Space Research* 42 (8): 6–17. doi:10.1016/j.asr.2008.01.017.

Urrutxua, H., D. Scheeres, C. Bombardelli, J. L. Gonzalo, and J. Pelaez. 2014. What Does it Take to Capture an Asteroid? A Case Study on Capturing Asteroid 2006 RH120. In *24th AAS/AIAA Space Flight Mechanics Meeting, Santa Fe, New Mexico, 26–30 January*, 1–20.

Vetrisano, M., W. Van der Weg, and M. Vasile. 2012. Navigating to the Moon along Low-Energy Transfers. *Celestial Mechanics and Dynamical Astronomy* 114 (1–2): 25–53. doi:10.1007/s10569-012-9436-9.

Yagasaki, K. 2004. Sun-Perturbed Earth-to-Moon Transfers with Low Energy and Moderate Flight Time. *Celestial Mechanics and Dynamical Astronomy* 90: 197–212. doi:10.1007/s10569-004-0406-8.